Supporting Information

Electrolyte additive enabling dual kinetic regulation for stable zinc anodes in aqueous zinc batteries

Huidi Shi [a], Yiqun Du [a,*], Liu Yang [b], Bingying Sun [c], Ximing Yu [b], Anbin Hu[a], Shuhua Yang [a], Jinkai Li [a], Bingqiang Cao [a,*]

[a] School of Material Science and Engineering, Shandong Provincial Key Laboratory of Photovoltaic Materials and High-efficiency Utilization Technology, University of Jinan, Jinan, China

[b] UJN–TWEG Joint Institute on Green Energy, TaiWei Energy Group, Jinan, China

[c] UJN–SDGE Joint Institute on Green Energy, Shandong Green Energy Investment Ltd, Jinan, China

*E-mail (Yiqun Du): mse_duyq@ujn.edu.cn

*E-mail (Bingqiang Cao): mse_caobq@ujn.edu.cn

Experimental Procedures

Preparation of electrolytes

Aqueous $ZnSO_4$ electrolytes were prepared by dissolving zinc sulfate heptahydrate ($ZnSO_4 \cdot 7H_2O$, Sigma-Aldrich) in deionized water. For the modified electrolytes, designated as $ZnSO_4$ + HB, varying molar ratios of 4-hydroxy-2-butanone (HB, Alfa Aesar) were introduced into the aqueous $ZnSO_4$ solution.

Electrode fabrication

MnO_2 powder was synthesized via a hydrothermal method. Specifically, 1 mmol of $MnSO_4 \cdot H_2O$ and 6 mmol of $KMnO_4$ were dissolved in 50 mL of deionized (DI) water under continuous magnetic stirring for 1 h to form a homogeneous precursor solution. The resultant mixture was transferred into a 100 mL PTFE-lined stainless steel autoclave and subjected to hydrothermal reaction at 150 °C for 24 h. After cooling to ambient temperature, the solid product was collected by vacuum filtration, repeatedly washed with DI water until neutral pH was achieved, and subsequently dried at 60 °C for 8 h in a convection oven.

For cathode fabrication, the as-synthesized MnO_2 powder (70 wt%), conductive carbon black (Super P, 20 wt%), and polyvinylidene fluoride (PVDF, 10 wt%) binder were mixed thoroughly in N-methyl-2-pyrrolidone (NMP) solvent to form a homogeneous slurry. This slurry was doctor-blade coated onto a 316L stainless steel current collector foil, followed by vacuum drying at 80 °C for 12 h. The active material mass loading (MnO_2) on the current collector was maintained at 2.0 ± 0.2 mg cm^{-2} for all CR2032 coin cell assemblies.

Electrochemical measurements

CR2025-type coin cells with Zn||Cu, Zn||Zn, and Zn||MnO_2 configurations were assembled employing zinc foil anodes (Ø 14 mm, thickness 100 µm), corresponding cathodes (Cu foil or MnO_2-coated substrates), glass fiber separators (Whatman GF/D, thickness 675 µm), and 80 µL electrolyte. For Zn||MnO_2 cells, 0.1 M $MnSO_4$ was incorporated into the $ZnSO_4$-based electrolyte to mitigate manganese dissolution.

Galvanostatic charge/discharge cycling was conducted using a CT-4008Q battery testing system. Comprehensive electrochemical characterization—including cyclic voltammetry (CV), Tafel polarization, linear sweep voltammetry (LSV), chronoamperometry (CA), and electrochemical impedance

spectroscopy (EIS)—was performed on a CHI 660E electrochemical workstation under controlled conditions.

CV measurements employed symmetric Zn||Zn cells scanned between ±15 mV at sweep rates of 2-10 mV s^{-1}. Tafel analysis was conducted in a three-electrode configuration where zinc foil served as both the working and counter electrode, along with a saturated Ag/AgCl reference electrode. Linear polarization was carried out at 1 mV s^{-1} in a 2 M $ZnSO_4$ electrolyte. LSV studies implemented a Ti mesh working electrode, graphite rod counter electrode, and Ag/AgCl reference in 2 M Na_2SO_4 electrolyte, sweeping at 5 mV s^{-1} from –1.5 to 0.5 V vs. Ag/AgCl. CA measurements applied a constant overpotential of –150 mV (±5 mV) to symmetric Zn||Zn cells. EIS spectra were acquired at open-circuit potential over 100 kHz to 10 mHz with 5 mV AC amplitude after 30 min equilibrium.

Characterizations

Raman spectra were acquired using a Horiba LabRAM HR Evolution spectrometer. Fourier transform infrared (FTIR) spectra were recorded on a Thermo Scientific Nicolet iS5 instrument, while nuclear magnetic resonance (NMR) measurements utilized a Bruker Avance NEO 400 MHz spectrometer. Structural and compositional analyses were performed via X-ray diffraction (XRD, Rigaku SmartLab 9KW, Cu Kα radiation) and X-ray photoelectron spectroscopy (XPS, Thermo Scientific ESCALAB Xineneneea+, Al Kα source). Morphological characterization was conducted using scanning electron microscopy (SEM, ZEISS GeminiSEM 360) and atomic force microscopy (AFM, Bruker Dimension Icon). For post-mortem analysis, Zn electrodes were extracted from symmetric cells after specific cycling conditions: either 100 cycles at 1 mA cm^{-2} and 1 mAh cm^{-2} or 50 cycles at 5 mA cm^{-2} and 5 mAh cm^{-2}. These electrodes underwent sequential rinsing with deionized water to eliminate residual electrolytes, followed by critical-point drying prior to SEM/AFM imaging. In situ optical visualization of zinc deposition behavior was implemented on 100-µm-thick Zn foils using a Sunny MX6R microscope equipped with a sealed electrochemical cell.

Theoretical calculations

In quantum chemical calculations, structural optimisation and accurate energy calculations were performed at the B3LYP-D3(BJ)/def2-SVP and M06-2X/def2-TZVP energy levels, respectively. The solute electron density (SMD) solvation model was used. The binding energy (Eb) between components A and B was determined by the formula $E_b = E_{\text{total}} - E_A - E_B$.

Results and Discussion

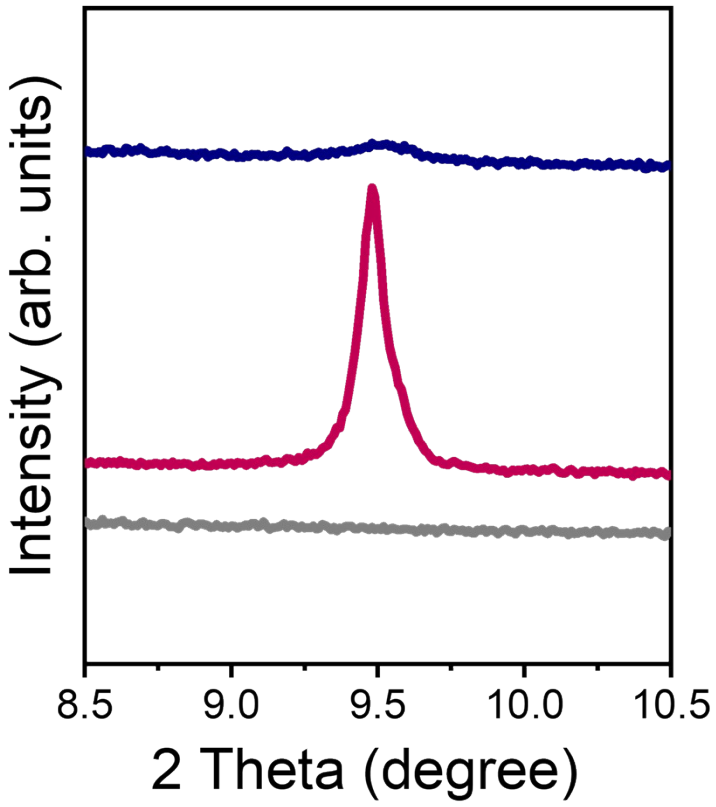

Fig. S1. XRD patterns of Zn electrodes before and after 100 hours of cycling at 1.0 mA cm^{-2} with 1.0 mAh cm^{-2}..

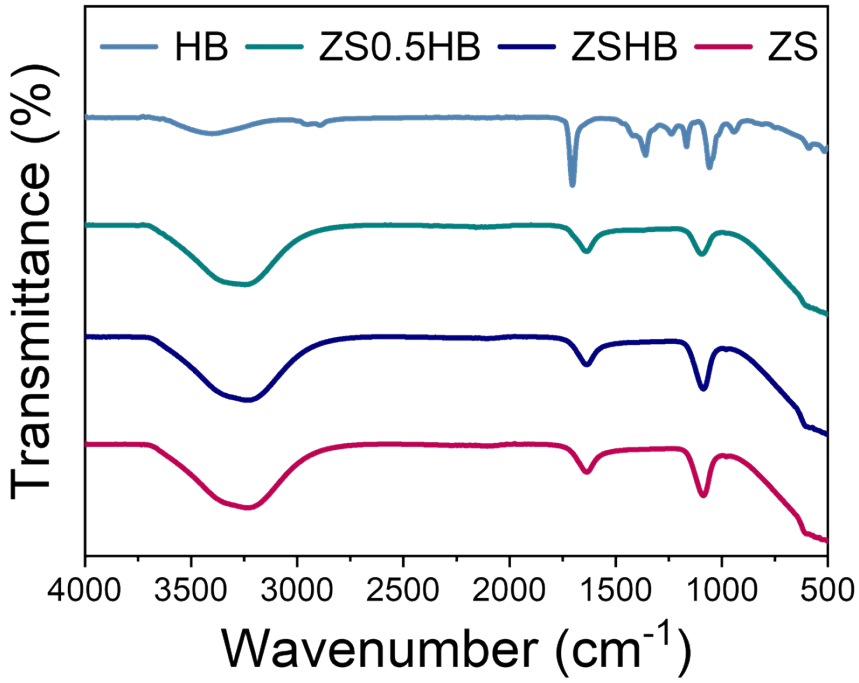

Fig. S2. FTIR.Electrolyte formulations comprised: (i) 0.5 M 4-hydroxy-2-butanone (denoted HB) and (ii) 1 M $ZnSO_4$ with 0.5 M 4-hydroxy-2-butanone (denoted ZS1HB).

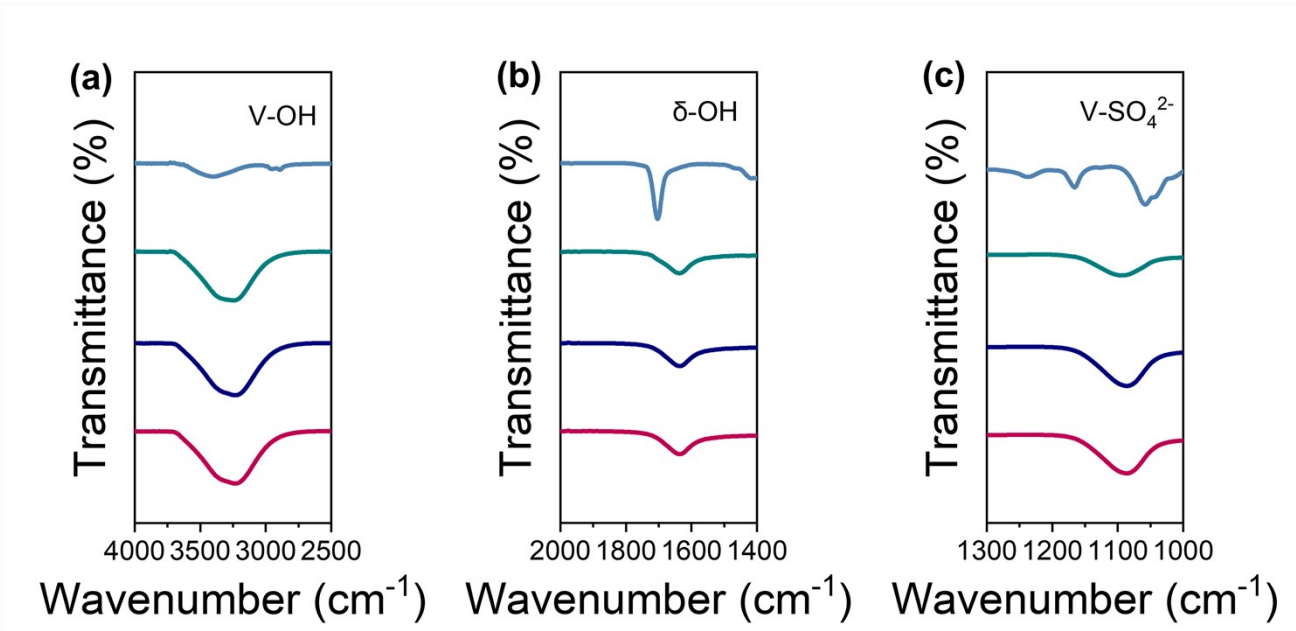

Fig. S3. a-c) Expanded View of the Specific Region in the FTIR Spectrum.

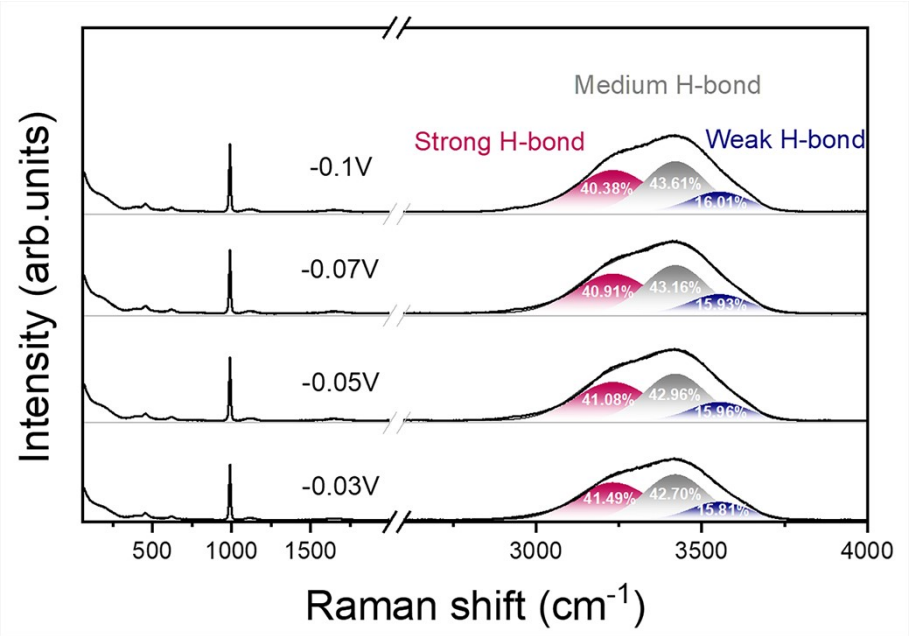

Fig. S4. Ex situ Raman spectroscopy at different voltages.

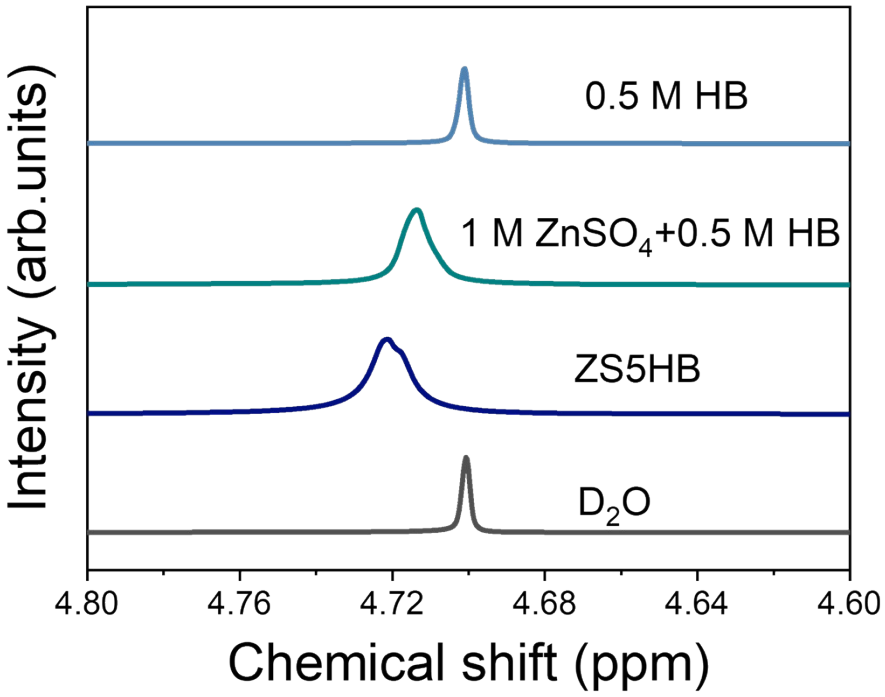

Fig. S5. NMR spectra for various solutions.

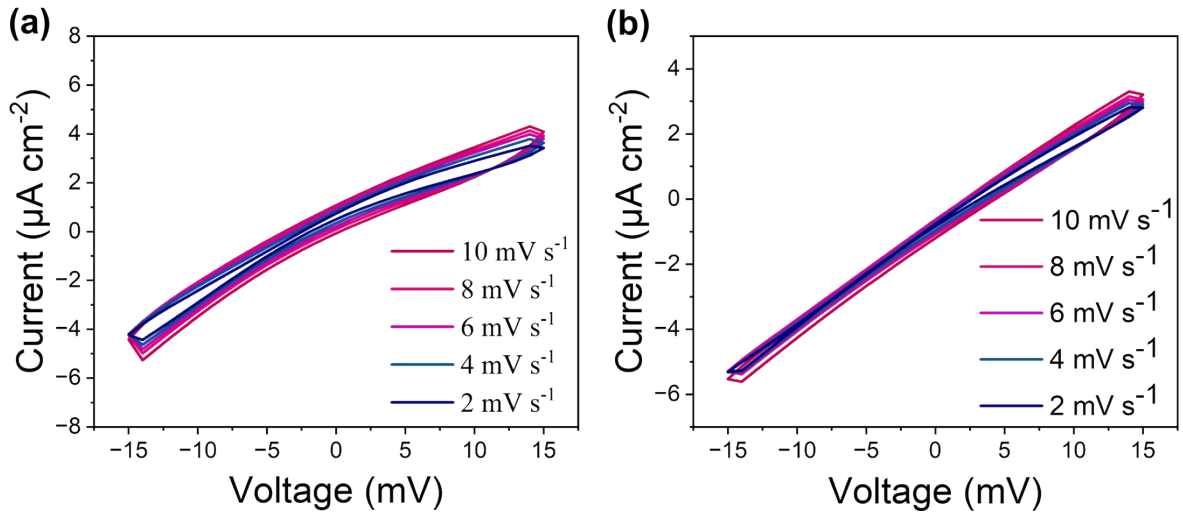

Fig. S6. CV curves of the Zn||Zn cells with a) ZS and (b ZS5NC between −15 mV and 15 mV under various scan rates.

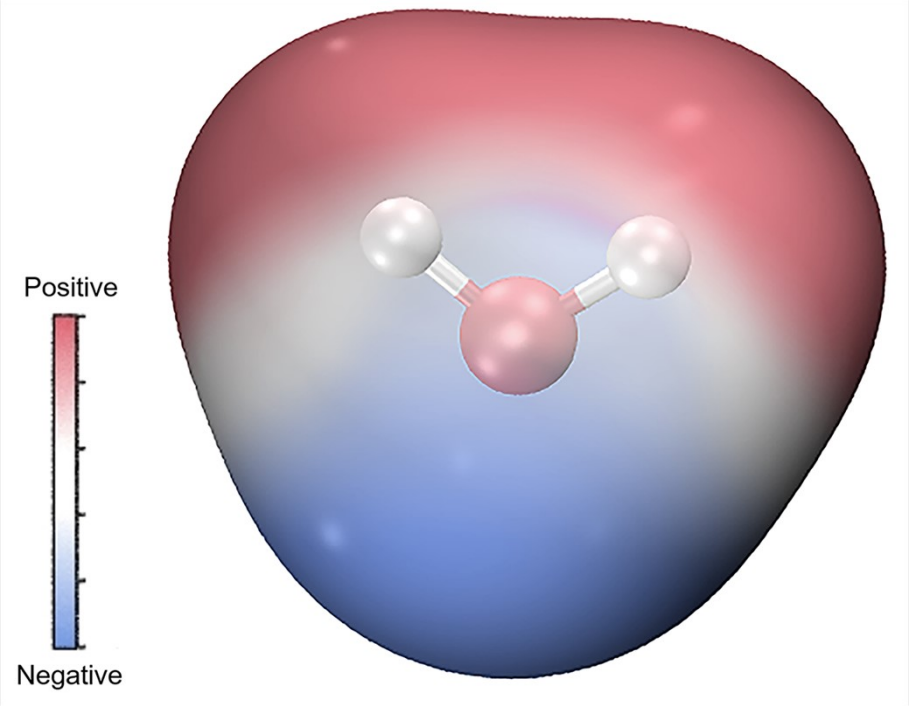

Fig. S7. The ESP map for H_2O.

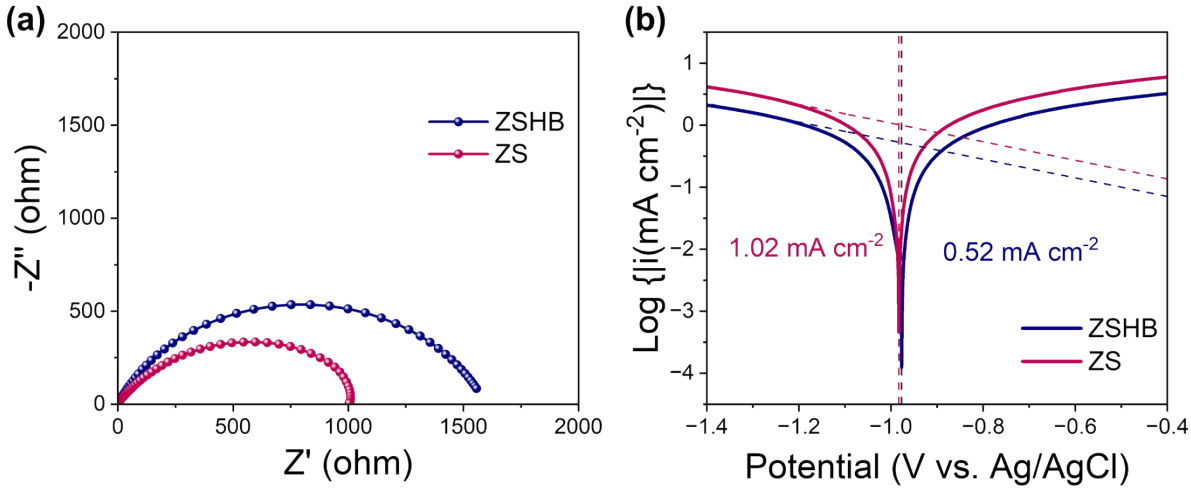

Fig. S8. a) Nyquist plots of Zn||Zn cells using ZS and ZSHB. b) Tafel plots at 1 mV s^{-1}.

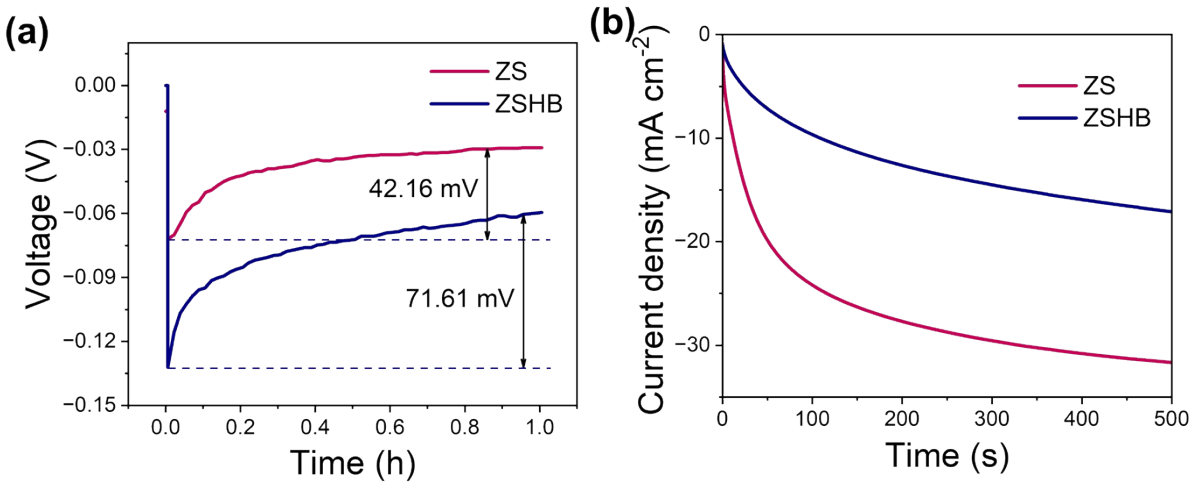

Fig. S9. a) Comparison of nucleation overpotentials for Zn||Zn cells using ZS and ZSHB electrolytes at 1.0 mA cm^{-2} and 1.0 mAh cm^{-2}. b) Chronoamperometry curves of the Zn||Zn cells at an overpotential of −150 mV.

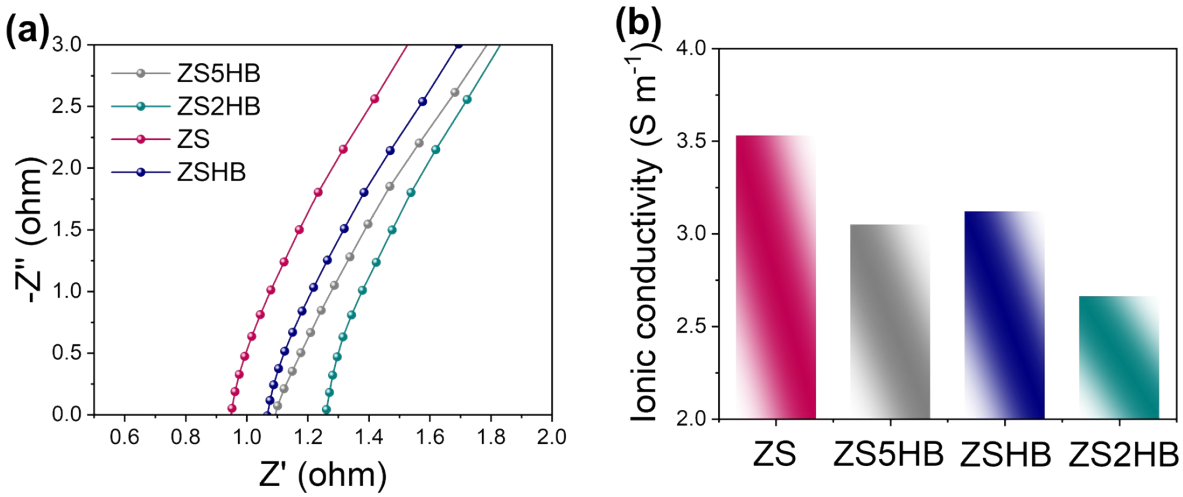

Fig. S10. a) Nyquist impedance plots and b) ionic conductivity of the electrolytes with different molar ratios.

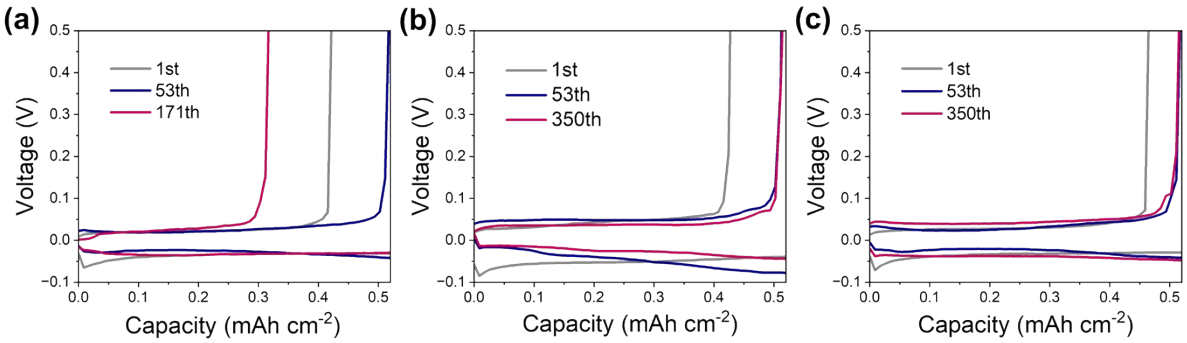

Fig. S11. a–c) Galvanostatic Zn plating/stripping curves for Zn||Cu cells employing a) ZS, b) ZS2NC, c) ZS5NC electrolytes at a current density of 0.5 mA cm^{-2} and an areal capacity of 0.5 mAh cm^{-2}..

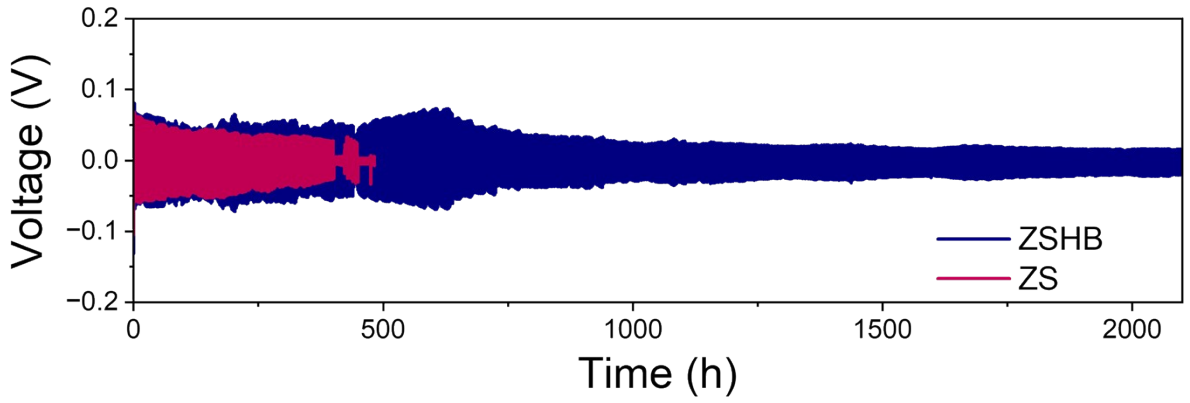

Fig. S12. Long-term cycling performances of Zn||Zn cells at 1.0 mA cm^{-2} and 1.0 mAh cm^{-2}.

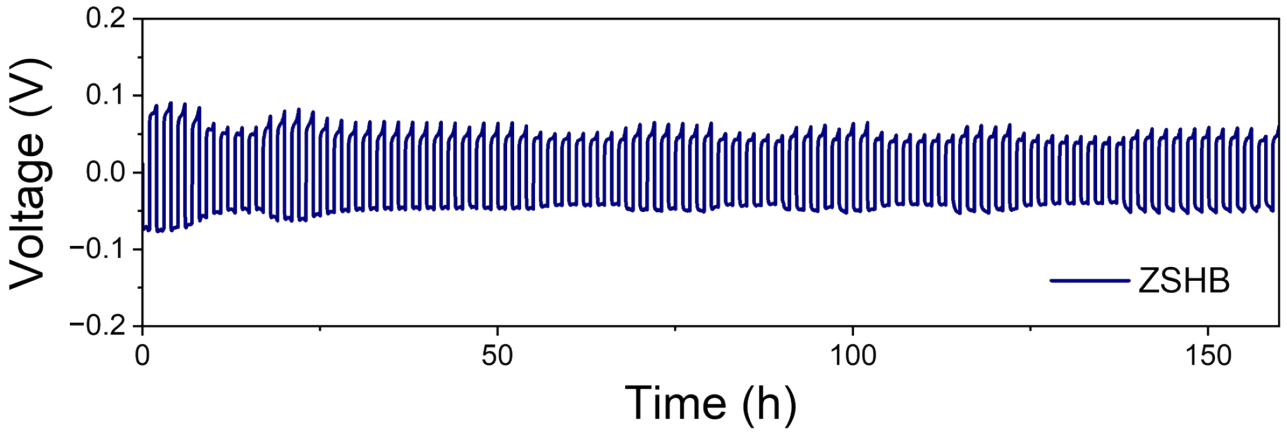

Fig. S13. Long-term cycling performances of Zn||Zn cells at 20 mA cm^{-2} and 20 mAh cm^{-2}..

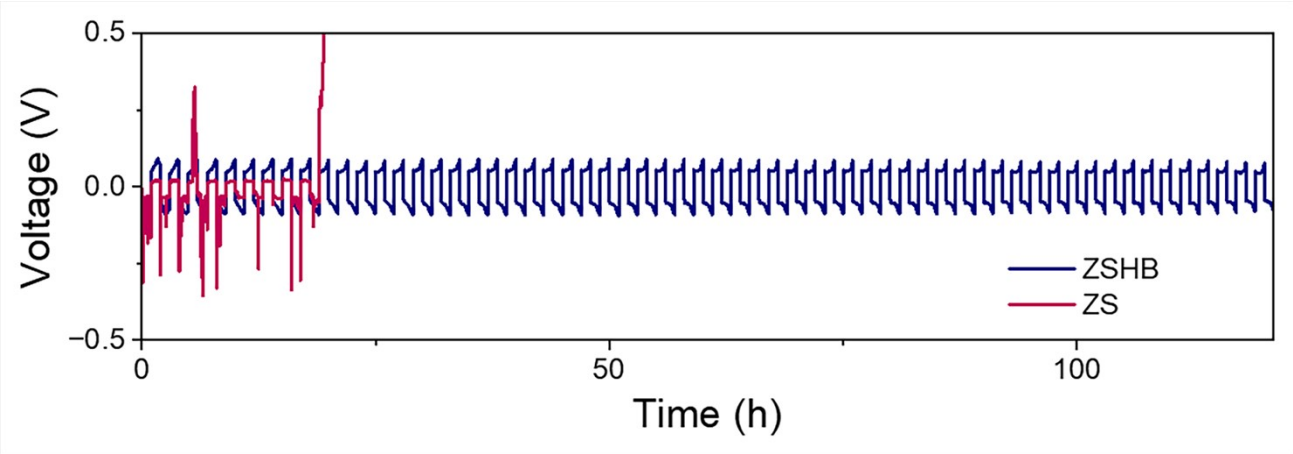

Fig. S14. Long-term cycling performances of Zn||Zn cells at DoD of 76%.

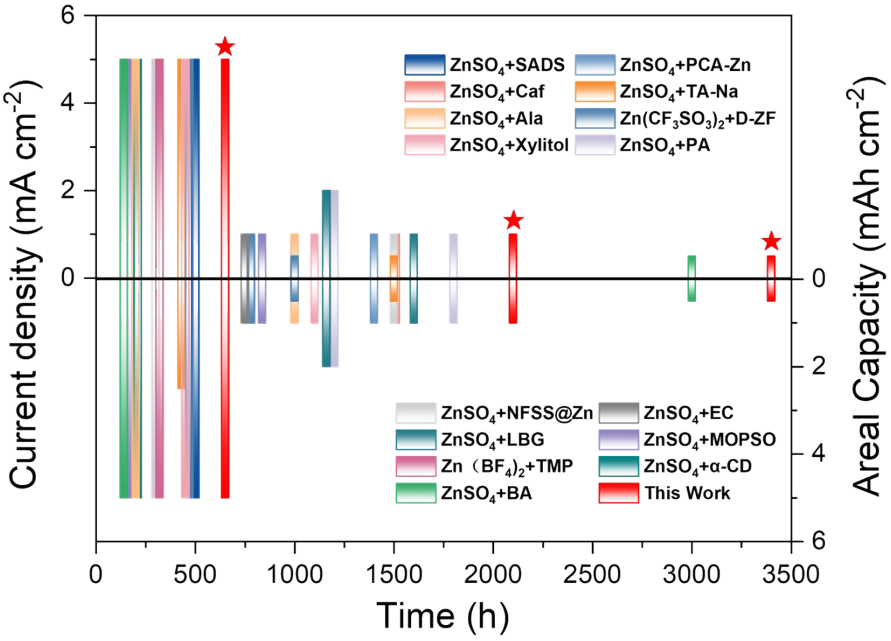

Fig. S15. Cycling stability comparison of Zn||Zn batteries with diverse electrolytes.[1-15]

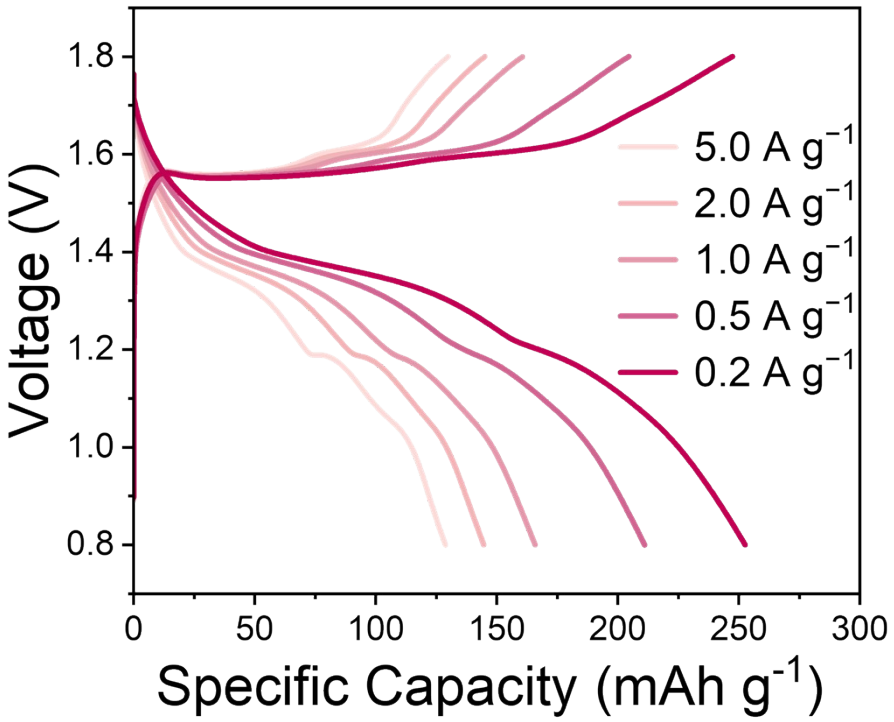

Fig. S16. Charge-discharge profiles at different current densities using ZSMS electrolytes.

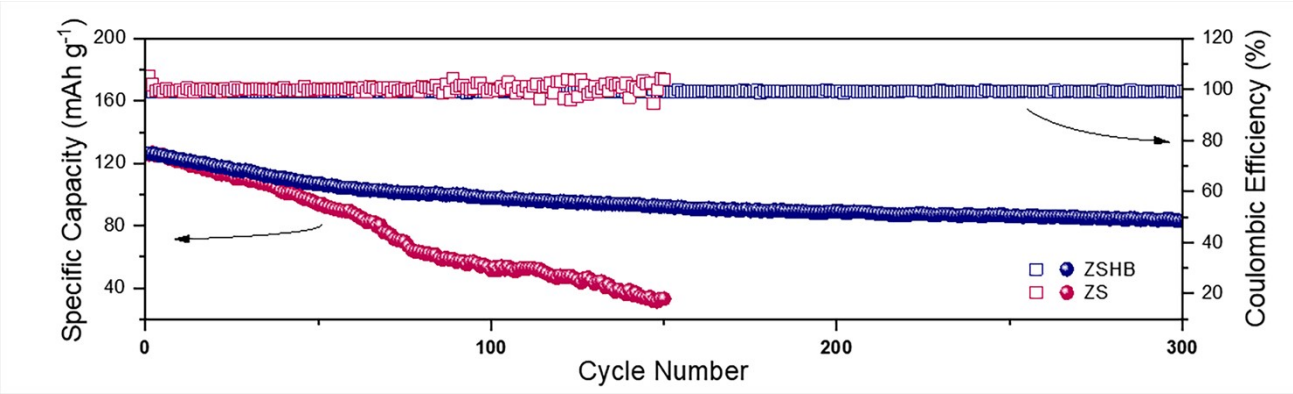

Fig. S17. The long-term cycling performance for the Zn||MnO2 battery with ZSHBMS electrolyte at a low N/P ratio of 4.75.

References

1. G. Ma, S. Di, Y. Wang, W. Yuan, X. Ji, K. Qiu, M. Liu, X. Nie and N. Zhang, *Energy Storage Materials*, 2023, **54**, 276-283.
2. K. Wang, H. Zhan, X. X. Liu and X. Sun, *Advanced Functional Materials*, 2024, **35**, 2418993.
3. Y. Ding, L. Yin, T. Du, Y. Wang, Z. He, J. A. Yuwono, G. Li, J. Liu, S. Zhang, T. Yang and Z. Guo, *Advanced Functional Materials*, 2024, **34**, 2314388.
4. N. Cai, H. Chen, B. Zhang, Z. Liu, X. He and D. Zhou, *Journal of Energy Chemistry*, 2025, **101**, 651-660.
5. H. Yang, K. Fang, J. Duan, J. Dong, Y. Li, S. Yang, J. Liang, Y. Jiang, M. Li, Y. Liu, Z. Shen, R. Liu, R. Cao, F. Li and Y. Huang, *Energy Storage Materials*, 2025, **75**, 103995.
6. B. Liu, C. Wei, Z. Zhu, Y. Fang, Z. Bian, X. Lei, Y. Zhou, C. Tang, Y. Qian and G. Wang, *Angewandte Chemie International Edition*, 2022, **61**, e202212780.
7. J. Duan, J. Dong, R. Cao, H. Yang, K. Fang, Y. Liu, Z. Shen, F. Li, R. Liu, H. Li and C. Chen, *Advanced Science*, 2023, **10**, 2303343.
8. S. jiao, J. Fu, Q. Yin, H. Yao and H. Hu, *Energy Storage Materials*, 2023, **59**, 102774.
9. K. Wang, H. Zhan, W. Su, X.-X. Liu and X. Sun, *Energy & Environmental Science*, 2025, **18**, 1398-1407.
10. H. Wang, W. Ye, B. Yin, K. Wang, M. S. Riaz, B. B. Xie, Y. Zhong and Y. Hu, *Angewandte Chemie International Edition*, 2023, **62**, e202218872.
11. K. Wang, Y. Luo, H. Zhan, X.-X. Liu and X. Sun, *ACS Nano*, 2024, **18**, 27672-27682.
12. J. Wan, R. Wang, Z. Liu, L. Zhang, F. Liang, T. Zhou, S. Zhang, L. Zhang, Q. Lu, C. Zhang and Z. Guo, *ACS Nano*, 2023, **17**, 1610-1621.
13. J. Li, Z. Guo, J. Wu, Z. Zheng, Z. Yu, F. She, L. Lai, H. Li, Y. Chen and L. Wei, *Advanced Energy Materials*, 2023, **13**, 2301743.
14. Z. Luo, T. Xu, L. Cao, Q. Liu, D. Li, X. Zhuge, L. Liu, Y. Li, K. Luo, K. Qi and B. Y. Xia, *Journal of Energy Chemistry*, 2025, **107**, 44-52.
15. K. Zhao, G. Fan, J. Liu, F. Liu, J. Li, X. Zhou, Y. Ni, M. Yu, Y.-M. Zhang, H. Su, Q. Liu and F. Cheng, *Journal of the American Chemical Society*, 2022, **144**, 11129-11137.